

Computational and Experimental Aeromechanics Analysis of a Coaxial Rotor System in Hover and Forward Flight

Roland Feil^{*} Jürgen Rauleder[†] Manfred Hajek[‡]

Institute of Helicopter Technology
Technical University of Munich, Germany

Christopher G. Cameron[§] Jayant Sirohi[¶]

University of Texas at Austin, TX, USA

The dynamics and aerodynamics of a coaxial rotor model designed for high-advance-ratio forward flight were investigated by means of a numerical comprehensive analysis, hover and wind tunnel testing. The focus was on the development of the computational model and its validation using wind tunnel measurements for advance ratios of up to 0.5. Blade structural characteristics were modeled according to the measured elastic properties and reduced-order aerodynamics modeling using a free vortex wake method was used to ensure computational efficiency. Numerical predictions for the coaxial rotors correlated well with the measurements for performance, blade loadings, cyclic controls, and blade clearance for multiple advance ratios and varying lift-offset conditions, and particularly well for medium to high advance ratios ($\mu = 0.3 - 0.5$). Differences at high lift-offset conditions may be related to an underprediction in the lateral cyclic controls. Vibratory hub loads correlated well with the measurements in both trends and magnitudes for the isolated rotor. For the coaxial configuration, the same good agreement was found in the axial vibratory loads, while drag and side forces only captured the trends seen in the experiments that also showed significant higher-frequency content. The validated low-order modeling capabilities will be helpful to quickly assess the rotor dynamic response and its aerodynamic sources, including the effects of lift offset and rotor-rotor interactions, and so they will prove instrumental in the understanding of the steady and vibratory loads in the present test article as well as in future coaxial rotor designs.

NOMENCLATURE

CAMRAD II	Comprehensive Analytical Model of Rotorcraft Aerodynamics and Dynamics	T	rotor thrust, N
C_{MX}	roll moment coefficient, $M_X/(\rho\pi\Omega^2R^5)$	U, L	Upper and Lower rotor index
C_T	thrust coefficient, $T/(\rho\pi\Omega^2R^4)$	UMARC	University of Maryland Advanced Rotorcraft Code
F_X, F_Y, F_Z	rotor hub forces for drag force, side force and axial force, respectively, N	V_{tip}	rotor blade tip speed, ΩR , m/s
F_{Xn}, F_{Yn}, F_{Zn}	harmonic hub loads for drag force, side force and axial force, respectively, N	V_∞	wind speed, m/s
FWW	Free Vortex Wake	c	rotor blade chord, m
LO	lift offset, %	r_{rc}	radial station of root cutout, m
M_X	rotor roll moment, Nm	β_p	precone angle, deg
N_b	number of rotor blades	$\Theta_0, \Theta_{1s}, \Theta_{1c}$	collective and cyclic controls, deg
R	rotor radius, m	μ	advance ratio, $V_\infty/(\Omega R)$
		ρ	air density, kg/m^3
		σ	rotor solidity, $N_b c/(\pi R)$
		ψ_b	rotor blade azimuth angle, deg
		Ω	rotor angular velocity, RPM

^{*} Graduate Research Assistant. roland.feil@tum.de

[†] Assistant Professor. juergen.rauleder@tum.de

[‡] Professor and Department Head. hajek@tum.de

[§] Graduate Research Assistant. c.cameron@utexas.edu

[¶] Associate Professor. jayant.sirohi@mail.utexas.edu

Presented at the 42nd European Rotorcraft Forum, Lille, France, September 6–8, 2016. Copyright ©2016 by the authors except where noted. All rights reserved. Published by CEAS with permission.

1. INTRODUCTION

Current vertical-takeoff-and-landing aircraft designs are generally a compromise between efficient hover performance and forward flight performance. With both high-speed capability and range being important future requirements, the aforementioned compromise is even more of a challenge. Whereas tiltrotor aircraft have extended range

and good high-speed performance, their hover performance is, in general, inferior to that of helicopters because of their high disk loading [1]. Conversely, fast edgewise flight of the helicopter is mainly limited by the asymmetric aerodynamics at the rotor disk and associated retreating blade stall.

One concept to overcome the forward flight speed limitations imposed by retreating blade stall is by off-loading the retreating blade from its requirement to balance the lift that is generated on the advancing side of the rotor disk. Thereby, the full lift potential of the advancing blades can be realized, allowing them to operate at angles of attack closer to their optimum, thus also attaining better performance at high forward speeds. This can be accomplished by two counter-rotating rotors in coaxial configuration (see, e.g., Fig. 1), such that most of the lift is produced by the advancing blades of each rotor while maintaining roll moment trim.

High-speed-capable coaxial rotor systems have gained increased attention in recent years [2]. From an experimental research perspective, Coleman [3] gave an overview of previously performed measurements on coaxial rotor systems, and Ramasamy [4] conducted a more recent experimental study into the influence of interactional aerodynamics of different rotor systems (including coaxial rotors) on the power requirements.

The majority of the work on coaxial rotor systems utilizing lift offset has been done using analytical models of various levels of fidelity. Some of the effects of the level of sophistication of such models on the computational predictions are found in [5], including validation by subscale rotor test data. Previous analytical work has been conducted on the aerodynamic interactions of upper and lower rotors of coaxial systems using free vortex wake aerodynamics modeling [6].

Comprehensive analysis models have been used to include the effects of structural dynamics using lower-order aerodynamics modeling, investigating the effects of lift offset and blade loading on rotor performance [7, 8]. Coupled computational fluid dynamics/computational structural dynamics (CFD/CSD) analyses have also been conducted [9, 10] using higher-fidelity (RANS) CFD modeling for the aerodynamics and comprehensive rotor codes for the blade motion (i.e., flapping and lead-lag motions) and structural dynamics. However, higher-order aerodynamics modeling does not necessarily improve the correlation (to measurements) and any numerical prediction still needs validation by experiments.

Recently, experiments have been performed for a high-advance-ratio coaxial model rotor system in hover [11, 12] and also in a wind tunnel [13], and comprehensive analysis has been done for the same (approximately 2m diameter) rotor system [14, 15]. However, there is still limited knowledge of the interactional aerodynamics, structural dynamics, and flight dynamics of rotorcraft with coaxial rotor systems, particularly at high advance ratios. Therefore, more

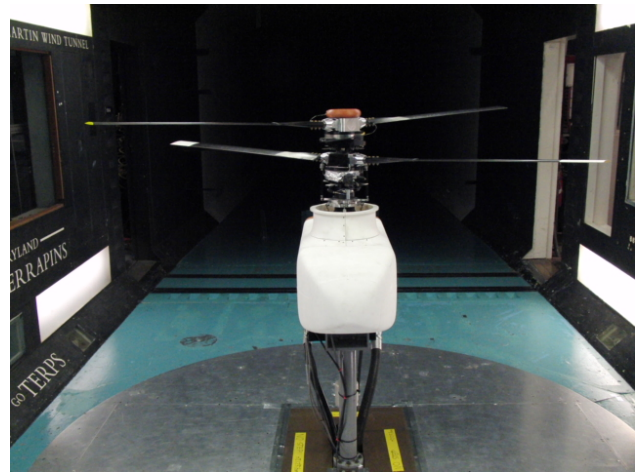


Fig. 1: 2x2-bladed coaxial rotor system in the Glenn L. Martin Wind Tunnel at the University of Maryland.

research is needed into these specific areas of interest to provide more insight, to better understand the unsteady forces/loads and their aerodynamic and dynamic sources, to produce a real (validated) predictive capability for these challenging rotor systems, and ultimately, to enable technology and performance improvements.

Rigid rotors are one key technology enabler for coaxial rotor systems that are capable of high forward flight speed. The suppressed (or at least significantly reduced) flapping motion of the rotor blades allows for smaller rotor spacing and so for significant hub drag reduction [16,17]. However, there is still little understanding as to the increased structural loads that are produced by such rigid rotors, including the effects of unsteady loads on the blades, rotor mast, pitch links, and other components. Furthermore, aerodynamic interactions between the upper and lower rotors, blade deflections and their effects on blade clearance are not well understood and they require further research.

To this end, in the present work, a collaborative effort is described using computational modeling together with hover and wind-tunnel tests to validate the modeling approach. A detailed level of structural modeling of the rotor blades and control system was used within a comprehensive aeromechanics analysis framework using lower-order aerodynamics modeling to ensure computational efficiency. The predictive model was validated in hover and in forward flight conditions at several advance ratios by a comparison to the performed measurements that were obtained on a hover tower and in a wind tunnel, respectively.

2. DESCRIPTION OF THE EXPERIMENTS

Experiments were performed on a 2 m diameter, rigid coaxial, counter-rotating rotor system. Details of the experimental setup are given in [11, 12], and a summary of the rotor dimensions and operational parameters is given in Tables 1 and Figs. 2 and 8. Data from hover tests performed by Cameron et al. [11, 12] were used to calibrate the analysis and validate the numerical predictions. The same rotor

system was also tested in forward flight at the Glenn L. Martin Wind Tunnel at the University of Maryland [13]; see Fig. 1. Steady and vibratory upper and lower rotor hub loads, upper and lower rotor pitch link loads as well as blade clearance were measured at over 400 test conditions, up to an advance ratio of 0.5 and a lift offset of 20%. Measurements were performed at a rotor speed of 900 RPM at all test conditions to maximize the test envelope in terms of allowable blade clearance. Some test conditions were repeated at 1200 RPM to investigate the effect of Reynolds number on the measured data. No statistically significant difference was found between data measured at 900 RPM and 1200 RPM. Therefore all experimental and numerical data reported in this paper corresponds to a rotor speed of 900 RPM.

Table 1: Rotor parameters.

Parameter	2-bladed	Coaxial
N_b	2	2x2
R , m	1.016	1.016
r_{rc} , m	0.122	0.122
Inter-rotor spacing	-	0.140 m (13.8 %R)
Airfoil section	VR-12	VR-12
β_p , deg	3	3
c , m	0.080	0.080
σ	0.05	0.1
V_{tip} , m/s	95.76	95.76
Ω , RPM	900	900

Fixed-frame instrumentation

Fixed-frame instrumentation included a two axis MEMs accelerometer to measure the vibration of the transmission. A 4096/revolution incremental encoder mounted on the motor drive shaft measured azimuth angle and was used to synchronously average all measurements over 100 revolutions at each test case. Data was transmitted through electrical slip rings and was acquired using a pair of National Instruments PXI-6358 simultaneous sampling, multifunction DAQ cards at 16 bits resolution and a sampling frequency of 30 kHz.

Loads measurement

The hub loads on the upper and lower rotors were measured using custom modified, six-component load cells mounted between each rotor hub and rotor shaft. The resolution of force and moment measurements was 0.75 N and 0.025 Nm respectively. In plane forces were measured with a bias accuracies of 4 N, while the thrust was measured with bias accuracy of 8 N. All moment measurements had bias accuracies of 0.5 Nm. The natural frequencies of the load cells were greater than 1000 Hz in all directions (without the hub and rotor mounted).

Push rod loads were measured using tension-compression load cells designed and fabricated in-house.

The push rod loads were necessary to correct the force and moment readings from the six-component load cells due to the load-path through the rotating frame. The push rod load cells were based on a full-bridge strain gauge instrumented hoop, with on-board signal conditioning. They had a full scale range of 250 N, with a calibrated bias accuracy of 0.5 N.

Pitch angle sensor

Individual blade root pitch angles were measured using linear Hall effect sensors located inside the upper and lower rotor hubs. Cubic polynomial calibrations accurate to $\pm 0.5^\circ$ were used for post-processing of the data.

Blade clearance sensor

An optical blade clearance sensor was located on the underside of an upper rotor blade, at a spanwise location of 90% radius. This sensor measured the clearance between the upper and lower rotor blades based on the intensity of reflected light. Calibrations performed in the non-rotating condition resulted in an uncertainty between 5-10 mm.

Control system

The upper and lower rotors were controlled by independent swashplates with electromechanical linear actuators. The upper rotor blade pitch control linkage had two sets of bell cranks and push rods that were located inside the upper rotor shaft. Due to the numerous linkages and joints, the free play in the upper rotor blade pitch angle was approximately $\pm 1.5^\circ$. The linear actuators themselves had a positioning accuracy of less than 50 μm . Because the blade pitch angle was measured directly at the blade root, any higher harmonics in the blade pitch angle were due to the free play in the control linkage.

Experimental error

At each test condition, data from 100 revolutions were recorded and post-processed in Matlab. First, a 36/rev notch filter was applied to the data to eliminate the spurious signal introduced by the 36 tooth drive pulleys. By treating each revolution as an independent, identically distributed sample, the mean values and standard deviation over 100 revolutions were calculated. For the vibratory signals, the time histories were resampled to the azimuthal domain using the encoder, and were then synchronously averaged. Total uncertainty was calculated as the square root of the sum of the squares of precision uncertainty and bias uncertainty. Precision uncertainty was determined using the standard error of the measurement, along with the appropriate statistics to estimate a 95% confidence interval on the mean. The bias uncertainty was determined using the

standard error of calibration curve fits for each sensor. Uncertainties for derived quantities, such as lift-to-drag ratio, were determined by error propagation of using sequential perturbation.

3. MODELING APPROACH

A comprehensive analysis of the presented rotor configuration was performed using CAMRAD II [18]. CAMRAD II is an aeromechanics analysis for rotorcraft that incorporates a combination of advanced treatments of rotating systems, including multibody dynamics, nonlinear finite element methods, and rotorcraft aerodynamics models. In this study, the rotor blade aerodynamics were modeled based on lifting line theory using steady two-dimensional airfoil characteristics. These airfoil characteristics of the VR-12 airfoil section were obtained from CFD computations for multiple Mach numbers and showed good correlation to experiments; see [15].

The aerodynamics model consisted of 22 aerodynamic panels along with 14 structural beam elements per blade. Unless otherwise noted, 24 azimuthal positions were calculated per rotor revolution. A computationally efficient free vortex wake (FVW) method was used to compute the rotor wake including complete interaction between the wakes of the two rotors. The free wake method discretizes the rotor wake into vortex filaments and then calculates the velocities induced by the filaments on each other and on the flow field using the Biot–Savart law [19, 20]. For example, Lim et al. [21] used a free vortex wake aerodynamics model and could satisfactorily correlate hover performance predictions from CAMRAD II to measured data from model-scale and full-scale coaxial rotors.

In the current FVW analysis, a multiple-trailer model with two trailers and vortex roll-up was used that previously showed good predictions of the lift distribution, vibrations, and tip vortex wake geometry [22]. Bagai–Leishman’s vorticity distribution [23], a Bagai–Leishman vortex core radius growth model [19] and a general free wake geometry allowed for rotor–rotor interactions to be accounted for. In order to sufficiently cover any form of blade–vortex or vortex–vortex interaction that affects the results, both the near and the far wake were truncated after ten revolutions of wake age with the wakes’ distortion being extended by another five revolutions of wake age. The shed wake was accounted for only in forward flight conditions.

For validation of the numerical model, measurements obtained with the previously described experimental setup were used. This recent setup with a cuffed blade geometry for the inboard sections (for additional stiffness) was tested in hover and also in high-advance-ratio conditions in the Glenn L. Martin wind tunnel at the University of Maryland, the latter marking the first-ever wind tunnel test of such a configuration, including measurements of vibratory forces and moments on the hub, pitch link loads, pitch angles, and blade deflections.

The rotor parameters of the experimental setup and the CAMRAD II model were identical; see Table 1. These (scaled) rotor parameters are similar to those of the Sikorsky X2 technology demonstrator [2], that successfully demonstrated high-advance-ratio flight. Therefore, the current setup is well suited to perform aeromechanics model validation of a coaxial rotor model designed for fast forward flight.

For the current aeromechanics model, the rectangular and non-twisted composite blades of the rotor had elastic properties according to Fig. 2. These blade elastic properties were obtained from static blade bending tests. Blade inboard sectional parameters were adjusted accordingly in order to match the non-rotating natural frequencies with measured data. This is a reasonable and physics-based assumption because, for mounting purposes, the blade had four holes at the inboard sections decreasing, e.g., the lag stiffness accordingly. Table 2 shows the control system’s main properties, including pitch horn length, pitch link

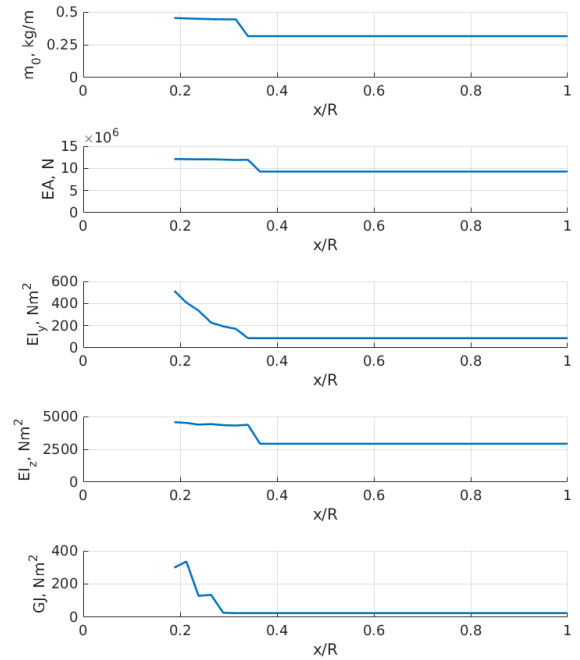


Fig. 2: Rotor blade spanwise structural properties.

Table 2: Control system parameters.

Parameter	Upper Rotor	Lower Rotor
Pitch horn length	0.013 m	0.0348 m
Pitch link stiffness	7.0×10^5 N/m	7.3×10^5 N/m
Swashplate below hub (Pitch link length)	0.873 m	0.1625 m

During hover, a six degree of freedom trim was used that is described in more detail in Ref. [24]. Now for the coaxial configuration, a five-degree-of-freedom wind tunnel trim (two degrees for the isolated rotor configuration) was used that independently varied the collective of the

lower and both cyclic controls of the upper and the lower rotor. The upper rotor's collective control is set as input for the wind tunnel condition and the other trim parameters are trimmed to the according flight condition. This trim algorithm provided the capability to individually target particular isolated rotor loads as well as total system loads, and it is the same control strategy as it is being used on the model rotor test setup. The five residuals for the coaxial trim algorithm were torque balance, and independent pitch and roll moments for each rotor. Trim convergence criteria was set to less than 0.1%. Note that, when talking about a set collective in the coaxial configuration, the upper rotor's collective pitch was set with the lower rotor being trimmed according to the described trim procedure.

The lift offset, LO , as illustrated in Fig. 3 with the thrust vector of an individual rotor being shifted in the coaxial system configuration, was calculated by

$$LO = \frac{C_{MX}}{C_T} \quad (1)$$

where C_T is the thrust coefficient and C_{MX} is the roll moment coefficient of the individual rotor. An average lift offset for the total coaxial system can also be defined by using the roll moments and thrust for both of the rotors:

$$LO_{COAX} = \frac{|C_{MX}^U| + |C_{MX}^L|}{C_T^U + C_T^L} \quad (2)$$

Figure 3 also shows the direction of rotation of the coaxial rotor system with the upper rotor rotating in counter-clockwise and the lower rotor rotating in clockwise direction.

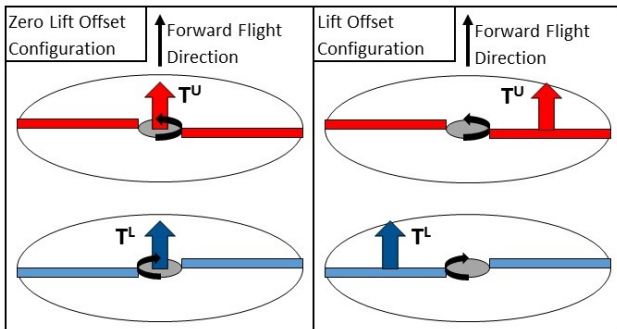


Fig. 3: Illustration of lift offset (red: upper rotor; blue: lower rotor).

4. RESULTS AND DISCUSSION

Validation of natural frequencies

The natural frequencies were determined experimentally for the non-rotating blade with a stiff mounting. Hence, only the structural elasticity of the blade itself may affect the modal behavior and the according natural frequencies. The elasticity of the control mechanism was omitted in this case. The CAMRAD II model was adapted accordingly in order to represent the test setup. The validated natural frequencies as well as the extended fan plot represent the dynamic characteristics of all the blades in the coaxial configuration.

Predicted natural frequencies were validated against non-rotating experimental test data for the first three flap (F) modes, the first lag (L) mode and the first torsion (T) mode; see Fig. 4. Table 3 summarizes the natural frequencies from the measurements for each mode along with the according standard deviation, and it also shows the CAMRAD II results for the validated non-rotating condition (at 0 RPM) as well as the nominal RPM of 900, and also a high RPM case of 1800, which was a test condition used for previous measurements not reported in this current work. Results were all well within their limits of the experimental standard deviation, even the third flap mode. At the nominal rotational speed of 900 RPM (i.e., the operating condition at which all of the results shown in this work were obtained), the predicted rotating natural frequencies did not coincide with the rotor harmonics (shown as black dashed lines in Fig. 4) and so structural resonance was not expected.

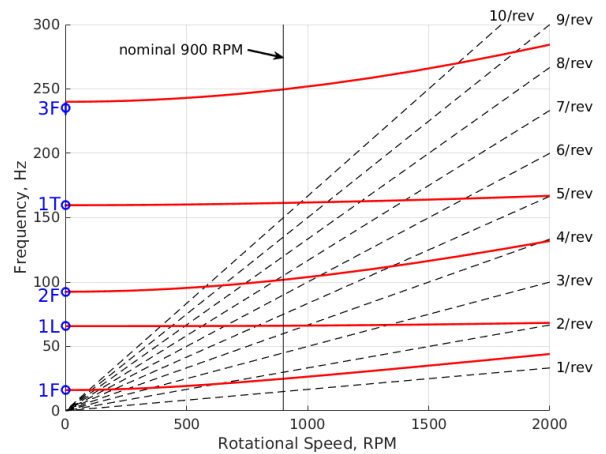


Fig. 4: Rotor blade fan plot.

Hover performance validation

Results in Fig. 5 show the hover performance for the isolated rotor case validated by experimental data from both the individual upper and lower rotors. The measurements from the lower rotor suggested that it had a slightly better

Table 3: Modal Frequencies in Hz.

Mode	Exp. frequency	Exp. standard deviation	CAMRAD II	CAMRAD II	CAMRAD II
	0 RPM	0 RPM	0 RPM	900 RPM	1800 RPM
1 st Flap	16.2	± 0.20	16.13	24.91	40.51
1 st Lag	65.8	-	65.79	66.09	67.79
2 nd Flap	92.5	±0.50	92.49	101.77	125.45
1 st Torsion	159.6	±1.00	159.70	161.45	165.71
3 rd Flap	235	± 5.00	240.00	249.64	276.53

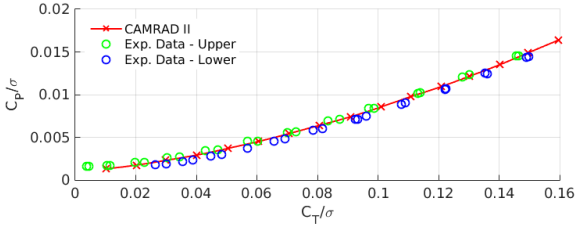


Fig. 5: Isolated single rotor hover performance.

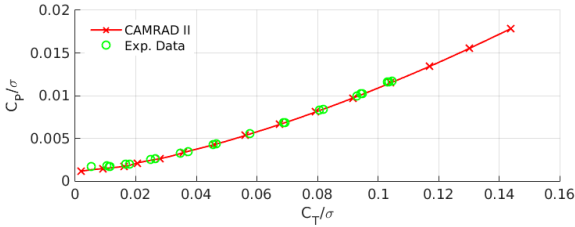


Fig. 6: Coaxial rotor hover performance.

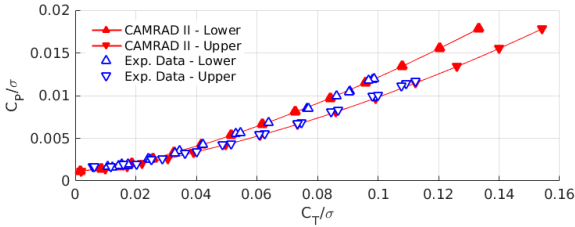


Fig. 7: Lower and upper coaxial rotor hover performance.

performance than the upper rotor. This behavior may be related to the lower rotor being closer to the dummy fuselage and, therefore, having increased aerodynamic interactions with the fuselage that are known to have a positive effect on rotor performance [1].

The CAMRAD II hover performance predictions showed good correlations to the power polars of both of the rotors. Because in the numerical simulation the fuselage was not included, the predictions were closer to the measurements obtained for the upper rotor (that was not influenced by the fuselage as much as the lower rotor). Figure 6 furthermore shows the total coaxial rotor performance in hover, while Fig. 7 shows the individual contributions of the lower and the upper rotors in the coaxial configuration. The individual as well as the total coaxial system performance correlated well with the experimental results.

Wind tunnel test data

Figure 8 shows the wind tunnel test envelope for a range of collective pitch angles and advance ratios. Collective pitch angles varied between 2° and 10°, and the advance ratio was constantly increased from 0.2 up to 0.5. From the test matrix (Fig. 8) it can be seen that test cases with a collective pitch of 8° were investigated for all rotor configurations (i.e., upper and lower isolated rotors as well as coaxial operation). Therefore, and because it provided realistically high blade loadings, the 8° collective case was used as the reference for lift-offset sweeps with multiple advance ratios in the analysis. For all shown cases, lift-offset conditions between 0 and 20% were tested, although the computational analysis was extended to include lift offsets of up to 25%. Besides the rotational speed of 900 RPM, further tests with the coaxial rotor system operating at 1200 RPM were conducted, but in this current comparative experimental/numerical study we focused on a rotational speed of 900 RPM.

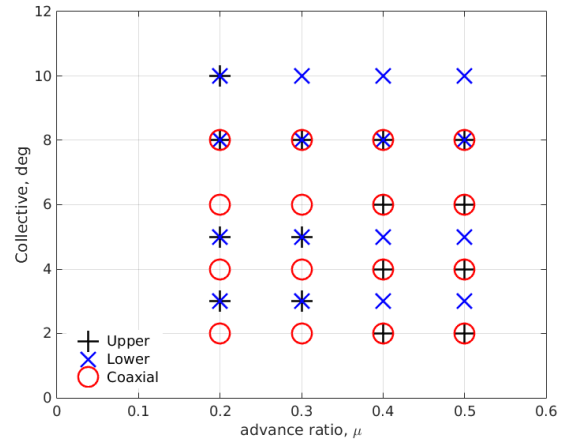


Fig. 8: Wind tunnel test envelope for isolated and coaxial rotor configurations at 900 RPM.

In the following forward flight analysis, it is first focused on the isolated rotor characteristics and thereafter the coaxial rotor configuration is analyzed, always validating the numerical analysis by wind-tunnel measurements. Experimental errors that were available for all data but for the cyclic controls are shown by error bars in the according data points within the figures. Because of challenges and uncertainties in the trim procedure, it was difficult to obtain exactly zero lift offset and exact controls in the ex-

periments. In the following, a nominal lift offset of the test data of zero indicates a lift offset between 0–5 %. The uncertainty in the collective pitch angles was $\pm 0.1^\circ$, i.e., a range of 7.9° to 8.1° for the 8° collective case.

Isolated rotor in forward flight

In this section, the isolated rotor results obtained with the CAMRAD II model that was described previously is examined together with according measurements from wind tunnel experiments. Both advance ratio sweeps and lift offset sweeps were performed for the isolated two-bladed rotor. Figure 9 shows the thrust that was predicted for set collectives and for a range of advance ratios. For low advance ratios such as $\mu = 0.2$, the thrust (or blade loading coefficient) was underpredicted, but it matched the experimental data well for the higher advance ratios. The blade loadings decreased from $\mu = 0.2$ to higher advance ratios. According to the predictions, this trend was reversed for low forward flight speeds at which the blade loading increased with increasing advance ratios (i.e., between hover and approximately $\mu = 0.2$ for the current model). Further experimental results at advance ratios between 0 and 0.2 are needed to validate this numerical result.

For the set collective pitch angles, the cyclic control inputs needed for trimmed forward flight were underpredicted by approximately 1° for both the longitudinal and the lateral cyclic pitch angles; see Figs. 10 and 11, respectively. This behavior did not significantly change with advance ratio or lift offset and remained at this constant offset of approximately 1° . Possible reasons for this constant underprediction for all test conditions may be related to the pitch angle sensor accuracy or the free play in the pitch angle control mechanism; see Chapter 2.

Notice that while Fig. 10 shows the longitudinal cyclic control over advance ratio for several collective pitch angles, Fig. 11 shows the lateral cyclic with varying lift offset for several advance ratios. Higher advance ratios needed more longitudinal cyclic control input, whereas greater lift offset required less lateral cyclic pitch input. Remember that by applying a certain lift offset the retreating blade is offloaded. Therefore, by having greater lift offsets, the retreating blade may be controlled by reduced lateral cyclic control angles. Note that when having a lift offset for an isolated (single) rotor, roll moment trim is no longer provided. Again, the trends were captured well for both the longitudinal and the lateral cyclic pitch, although a constant offset of approximately 1° in both control angles will require further attention and investigation.

Figure 12 shows the blade loading coefficient, C_T/σ , over a range of lift offsets up to 25% obtained for a set collective pitch angle of $\Theta_0 = 8^\circ$. Along with the numerical (CAMRAD II) predictions for the lower rotor, both the upper and the lower isolated rotor test results are shown. Good correlation was found for the lower rotor test results for medium to high advance ratios, such as 0.3 and 0.4,

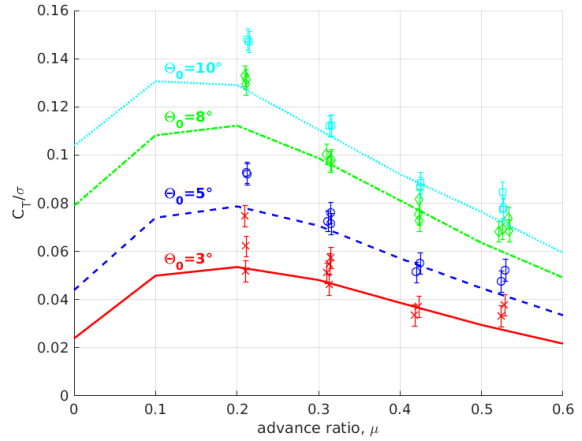


Fig. 9: Rotor blade loading coefficient versus advance ratio for the lower isolated rotor at multiple collective pitch angles and zero LO.

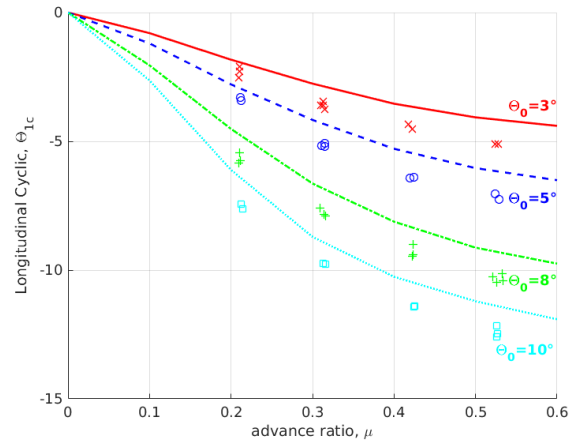


Fig. 10: Longitudinal cyclic control (in deg.) versus advance ratio for the lower isolated rotor at multiple collective pitch angles and zero LO.

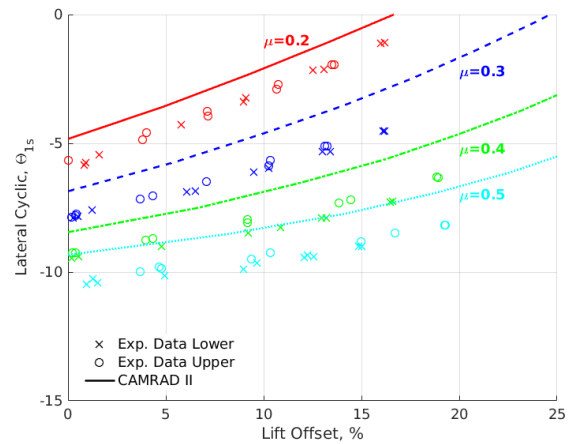


Fig. 11: Lateral cyclic control (in deg.) versus lift offset for the isolated rotor at multiple advance ratios at $\Theta_0 = 8^\circ$.

whereas the wind tunnel test data were underpredicted for the lower and higher advance ratios of 0.2 and 0.5, respectively. Test data as well as CAMRAD II results showed that by increasing the lift offset, the thrust (or blade loading) can be increased for a given collective pitch. This is due to the resulting thrust vector being shifted further to the advancing side and thereby offloading the retreating side; see Fig. 3.

Figure 13 shows the rotor drag, C_X/σ , for the isolated two-bladed rotors for varying lift offsets. The numerical results correlated well with the test data. For higher forward flight speeds (or advance ratios), the rotor drag increased less rapidly with increasing lift offset, which is a consequence from offloading the rotor from its lifting requirements on the retreating side of the rotor disk (to maintain roll moment balance) and rather taking advantage of the advancing side's lifting capabilities in the respective flight condition. The lower the advance ratio, the greater is the effect from an increased lift offset on the drag.

At low lift-offset conditions, a high-advance-ratio case obviously gave greater drag than a flight condition with a lower advance ratio; see Fig. 13. However, at higher lift-offset conditions this trend was reversed. Conversely, when applying a very high lift offset to a rotor that operates at low advance ratios, the (low forward speed) rotor drag may even exceed the drag at higher advance ratios (for the same lift offset) because the rotor operated well below its optimum lift to drag ratio in this case, whereas for high-advance ratios a high lift offset gave a benefit. Of course, the optimum combination of lift offset and advance ratio will depend on the rotor system and thrust levels.

The rotor side force, C_Y/σ , for several advance ratios and lift offsets is shown in Fig. 14. Although the general trends were predicted, the magnitudes of the side force were significantly underpredicted compared to the experiments. This is an interesting outcome from the CAMRAD II analysis, as similar trends and magnitudes were found using a different analysis (UMARC) [15]. These discrepancies between the two different comprehensive numerical analyses and the measurements require further attention and they will be investigated both from an experimental and numerical side.

The effects of high advance ratios on the distribution of the according angles of attack over the rotor disk area are shown in the predictions in Fig. 15, for a hover case on the left and a high-advance-ratio forward flight case on the right. Note that for reasons of visual clarity, the ranges in angle of attack were chosen independently for the two cases. An isolated rotor in hover has a completely uniform distribution of angles of attack; see Fig. 15a. However, at high advance ratios and zero lift offset, the roll moment trimmed isolated rotor may be exposed to a significantly large area of reverse flow and/or stall on the retreating side; see Fig. 15b. The airfoil tables applied in the analysis show stall limits at medium Mach numbers at angles of attack of approximately 13° . Hence, the region around $\psi_b = 270^\circ$

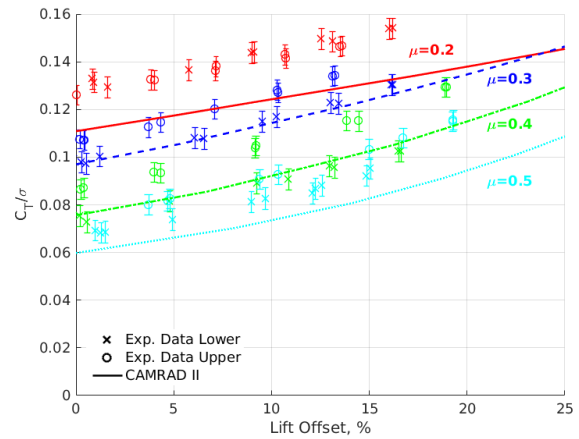


Fig. 12: Rotor blade loading coefficient versus lift offset at $\Theta_0 = 8^\circ$.

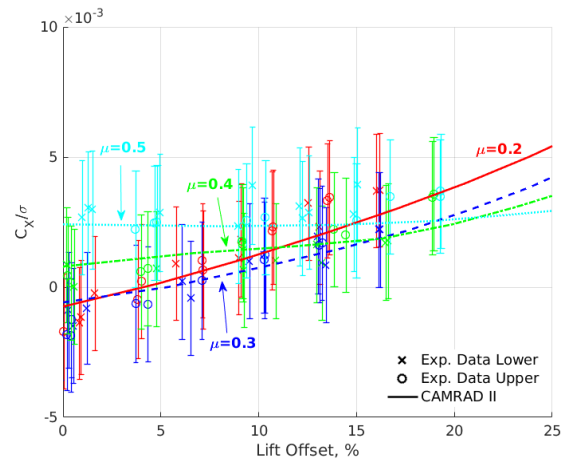


Fig. 13: Rotor drag versus lift offset at $\Theta_0 = 8^\circ$.

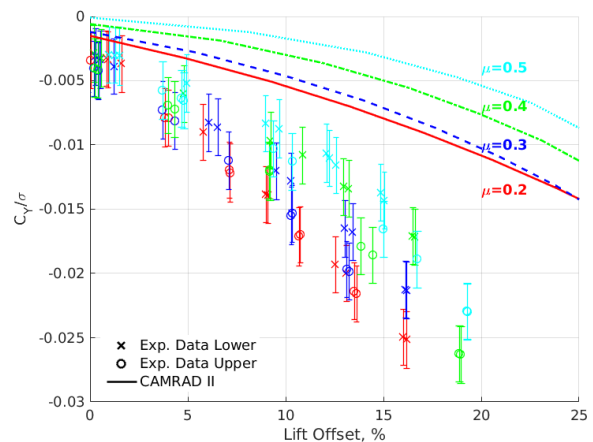


Fig. 14: Rotor side force versus lift offset at $\Theta_0 = 8^\circ$.

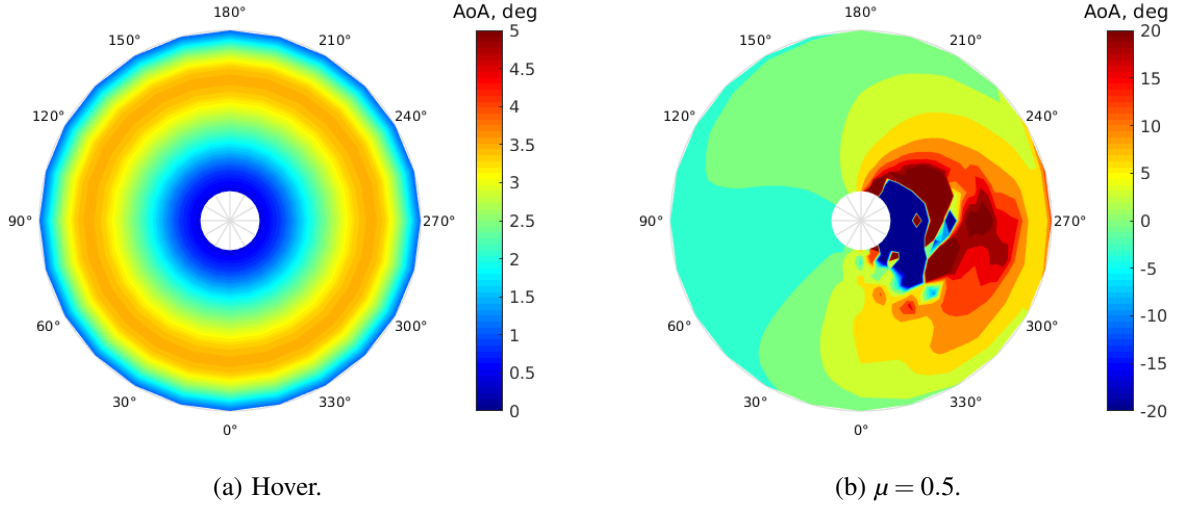


Fig. 15: Blade sectional angle of attack (in deg.) for the lower isolated rotor at $\Theta_0 = 8^\circ$ for hover and high-advance-ratio forward flight condition with zero lift offset, respectively.

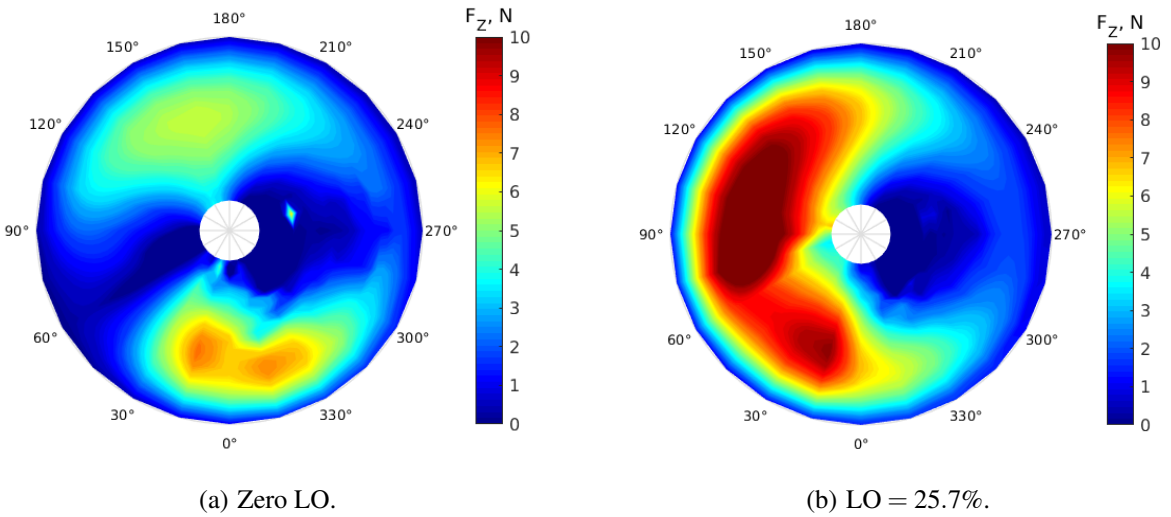


Fig. 16: Axial hub forces (in N) for the lower isolated rotor at $\Theta_0 = 8^\circ$ and $\mu = 0.5$ for a zero and a high lift-offset condition, respectively.

included reverse flow areas with negative angles of attack and stalled areas at high angles of attack.

To compensate for the reverse flow regions and the stalled regions on the retreating side of the rotor disk, higher angles of attack must be achieved at the outboard sections by applying increased lateral cyclic inputs to maintain roll moment trim. However, at such high advance ratios, the retreating blade is limited in its ability to produce enough thrust to counter the lift produced by the advancing side (for zero lift offset and roll moment trim). Therefore, in this case most of the thrust is produced in longitudinal direction, i.e., front and aft of the rotor disk ($\psi_b = 0^\circ$ and 180°); see Fig. 16. By initializing a certain lift offset at high advance ratios, the retreating blades are offloaded from the requirement to produce enough lift (or thrust) to maintain roll moment trim. Therefore, the resulting thrust vector is shifted further toward the advancing side, where

now most of the thrust is produced; see also Fig. 3. Note that the results in Figs. 16a and b were not obtained for the same thrust level but for the same collective pitch angle (i.e., $\Theta_0 = 8^\circ$) with targeted roll moments for lift offset initialization.

Coaxial rotor in forward flight

While the previous discussion was about the aeromechanics of the upper and the lower isolated rotor tests as well as the computational analysis on the lower isolated rotor, the following discussion is on the measurements and predictions of the coaxial rotor system.

Figure 17 shows the blade loading coefficient, C_T/σ , over the advance ratio for both the upper and the lower rotor when operating in the coaxial configuration at zero lift offset condition. Three collective pitch angles were in-

vestigated, with the collective always referring to the upper rotor's collective pitch angles that were prescribed for the trim routine, while the lower rotor's collective controls were then targeted to maintain torque balance. The general shape of the curves was similar to that from the isolated rotor(s) shown in Fig. 9, although the thrust contributions of the individual rotors were slightly lower in the coaxial configuration compared to the case when operated as single (isolated) rotors.

For low to medium advance ratios ($\mu = 0.2 - 0.3$), the measurements showed that the lower rotor produced significantly more thrust than the upper rotor, but this difference in thrust reduced significantly with higher advance ratios, where the numerical analysis correlated well with the measurements. Although the individual thrust contributions of the lower and upper rotor at low to medium advance ratios differed from the measurements, the resulting total (coaxial) system thrust was well predicted by the analysis, and the same characteristic trends with increasing advance ratios were seen.

Figure 18 shows the blade loading for varying lift offset. The upper rotor collective was set to $\Theta_0 = 8^\circ$ for the lift offset sweep analysis. Generally, there was good agreement between numerical predictions and the wind tunnel test data. However, as already found in Fig. 17, the thrust predicted for the individual rotors at lower advance ratios ($\mu = 0.2$ in this case) showed significantly different magnitudes compared to the measurements. One possible explanation could be that interference effects between the rotors were not modeled appropriately, or that the effects of the omitted rotor-fuselage interactions were greater than assumed (remember that the dummy fuselage was not modeled in the analysis). The thrust increased with greater lift offset for all investigated advance ratios. The low-speed case ($\mu = 0.2$) had a less steep and approximately constant slope. The reverse flow region at $\mu = 0.2$ was still relatively small, and for a collective of $\Theta_0 = 8^\circ$ the retreating blade was still able to produce sufficient thrust. As expected, primarily at low and medium wind speeds, the effect of lift offset increased with higher advance ratios.

For the wind-tunnel-trimmed coaxial rotor system, total system roll moment trim was always maintained. For non-zero lift offset, the upper rotor's roll moment counteracts the lower rotor's roll moment. Their signs are opposite with equivalent amplitudes. Figures 19 and 20 show the lateral and longitudinal cyclic controls with varying lift offset, respectively. Notice that the sign of the lower rotor's cyclic pitch angles was reversed to be able to show both rotors in the same graph. As expected, the magnitude of the lateral cyclic control angles must be increased for higher lift offsets to shift the resulting thrust vector further to the advancing side of the rotors and so offload the retreating side; see Fig. 3.

The predictions generally correlated well with the wind tunnel test data but tended to underpredict both of the cyclic pitch angles for upper and lower rotors for greater lift offsets ($LO > 10\%$). Greater lateral cyclic control was needed

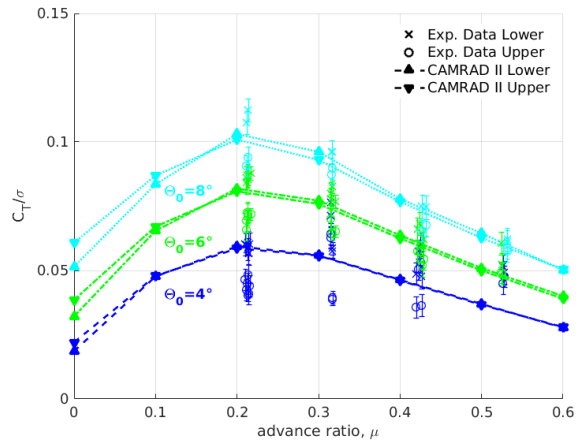


Fig. 17: Coaxial rotor blade loading coefficient versus advance ratio for zero LO.

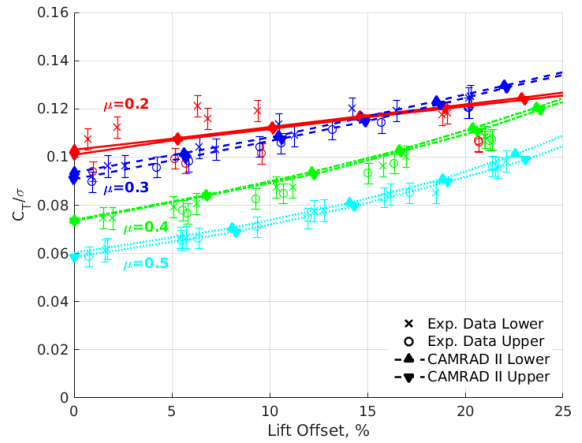


Fig. 18: Coaxial rotor blade loading coefficient over lift offset at $\Theta_0 = 8^\circ$.

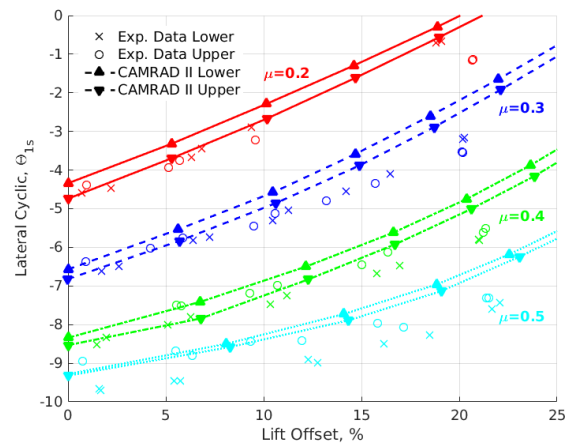


Fig. 19: Coaxial rotor lateral cyclic control (in deg.) over lift offset at $\Theta_0 = 8^\circ$.

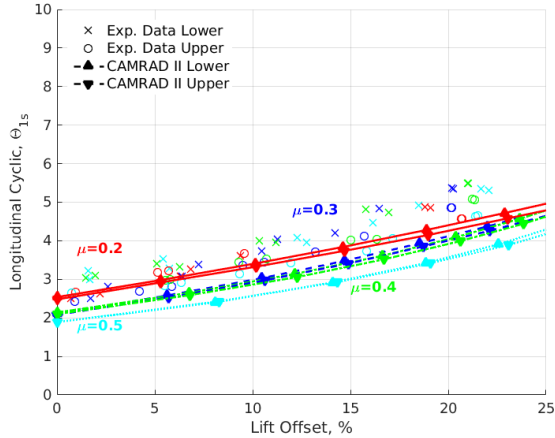


Fig. 20: Coaxial rotor longitudinal cyclic control (in deg.) over lift offset at $\theta_0 = 8^\circ$.

for increased advance ratios, as per definition the retreating blade must be pitched more at high forward flight speeds, the reasons being an increased area of reverse flow. In these flow regimes, zero or even negative lift may be produced. Longitudinal cyclic control angles (see Fig. 20) showed slightly increasing cyclic pitch input with greater lift offsets, whereas only small differences could be distinguished for varying advance ratio. Overall, the slopes of the longitudinal cyclic pitch angles with varying lift offset were approximately the same for various advance ratios, including an offset (or shift) to slightly smaller control angles for increasing advance ratios.

Figure 21 analyzes the minimum clearance between the upper and the lower rotor in the coaxial configuration for various operating conditions. The optical blade clearance sensor was installed on the upper rotor at approximately $0.9R$. Further information on the blade clearance sensor was previously given in the description of experiments section and can also be found in [13]. The virtual sensors used in the CAMRAD II model identified all four blade crossings during one revolution (similar to the experiments). The azimuthal positions where blade crossings occurred are shown in Fig. 22.

The results from the computational analysis predicted the minimal clearance at the 4th blade crossing, i.e., at a blade azimuth angle of $\psi_b = 270^\circ$ for the counter-clockwise rotating upper rotor (that was marked in red). At this location, the upper, retreating blade is flapping downward and the lower, advancing blade is flapping upward. At the 2nd blade crossing the maximum blade clearance was detected, a consequence from the respective blades flapping in opposite directions from what was described previously. The 1st and the 3rd blade crossings approximately measured the (non-rotating) inter-rotor spacing (see Table 1), i.e., the amount of blade bending of the upper and lower rotors was approximately equal in this case.

The predictions of the minimum rotor blade tip clearance, corresponding to the blade crossing at $\psi_b = 270^\circ$, were validated by the measurements for various lift offsets

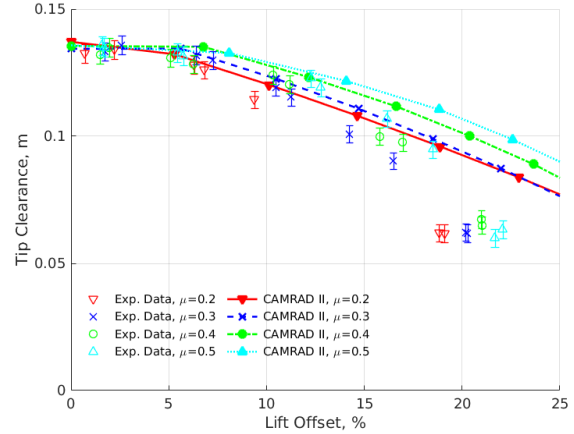


Fig. 21: Coaxial rotor tip clearance over lift offset.

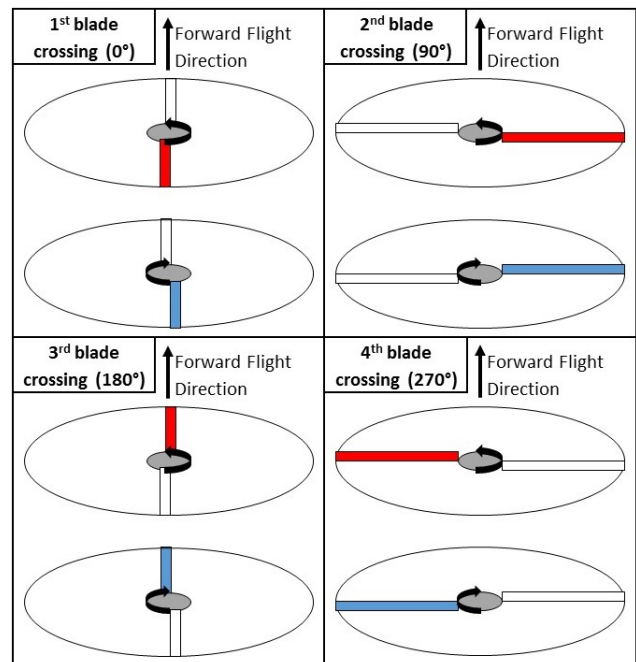


Fig. 22: Illustration of coaxial blade crossings at zero phase shift.

and advance ratios; see Fig. 21. These results give further confidence in the structural modeling of the elastic blades. Within the range of the estimated errors in the measurements, the results correlated well up to lift-offset values of approximately $LO = 15^\circ$. The differences in the tip clearance for greater lift offsets may be explained by the lower lateral cyclic controls that were predicted for the high lift-offset values (see Fig. 19), resulting in less cyclic flapping and so an overestimation of the tip clearance when compared to the wind tunnel measurements.

Vibratory hub loads

Vibratory hub loads were analyzed for the lower isolated rotor in forward flight at medium ($\mu = 0.3$) and high ($\mu = 0.5$) advance ratios for zero lift offset, and for both of the coaxial rotors at medium ($\mu = 0.3$) advance ratio with zero

lift offset, respectively. Notice that the experimental data also show the measurement uncertainties that were discussed previously in Section 2. In the analysis, the same wind tunnel trim procedure was used as in the wind tunnel measurements. In order to increase the resolution along the rotor azimuth, the number of azimuthal steps per rotor revolution was increased to 48/rev in the numerical analysis for better vibratory load determination. The harmonic results represent the same amplitude as in the time domain, showing the vibratory contributions in the frequency domain.

Figure 23 shows the time domain and Fig. 24 shows the frequency domain for the lower isolated rotor results for two advance ratios and for all three directions of the (measured and predicted) forces: drag force (longitudinal), side force (lateral), and lift force (axial). Focusing on the vibrations, only the results with the mean values removed are shown. Compared to the measurements, the CAMRAD II predictions showed similar characteristics and correlated well for all of the three forces and for both of the examined wind tunnel speeds (or advance ratios). The azimuthal peak positions were matched and the peak amplitudes correlated generally well.

As for the frequency content, the analysis slightly over-predicted the 2nd harmonics of all the forces for both advance ratios that are shown, although the correlations are still quite good between measurements and predictions. For the axial forces, the 2nd harmonics were predominant in this (isolated rotor) two-bladed configuration, whereas for the drag and side forces, the 4th harmonics had the predominant contributions. Note that there were fluctuations in the measurements (particularly the uneven harmonics) that also contributed to the vibrations. These effects can partly be explained by dissimilarities between the blades in terms of mass distribution resulting in a slight rotor imbalance that produced additional harmonics in the experiments, particularly in the first two harmonics. Furthermore, it was difficult to visually track the rotor blades because the rigid rotor hub and stiff rotor blades resulted in small tip deflections.

Figures 23b and 24b show the high-advance-ratio results at $\mu = 0.5$ for the isolated rotor in the time and frequency domain, respectively. At such high forward flight speeds the numerical prediction capability seems to get even better, with improving correlations in azimuthal positions and magnitudes. For drag and side force, smaller local maxima (higher frequency content) could not be predicted. However, for the axial force, some of these local peaks were predicted, i.e., at approximately 0° and 180°. Perhaps an even higher spatial resolution would help to further improve these results but besides increasing the computational time, it may also complicate the compliance with the numerical convergence criteria.

The coaxial rotors' vibratory hub loads are shown in Figs. 25 and 26. In this case, a flight condition at $\mu = 0.3$ with zero lift offset is shown, with $\Theta_0 = 8^\circ$ as the representative upper rotor collective pitch setting (for the trimmed,

torque-balanced coaxial rotor system). For the coaxial configuration, more higher harmonics and increased fluctuations in the time domain are apparent, particularly in the drag and side force wind tunnel data. These higher-frequency oscillations were not captured by the numerical analysis for neither upper nor lower rotor (see Fig. 25), and their origin first needs to be understood from an experimental point of view. However, the predominant 2/rev content in the axial (lift) force was predicted well for both rotors in the coaxial configuration, which is apparent both in the time domain and in the frequency domain; see Figs. 25 and 26, respectively.

With the exception of the side force, the frequency content of the 4th harmonic correlated also very well with the measurements; see Fig. 26. The discrepancy between the numerical and experimental results for the vibratory side force shown in Fig. 25 and for the side force versus lift offset shown previously in Fig. 14 require further investigation, both from an experimental and numerical perspective. Numerical drag characteristics were in good agreement with experimental data for the 2nd and 4th harmonics, but the experimental data also had significant 1/rev content as well as further higher harmonics, which made it challenging to properly validate the predicted vibratory hub loads in the time domain. The coaxial configuration showed significantly more (small amplitude) excursions in the wind tunnel test data compared to the results from the isolated rotor (compare Figs. 23 and 25) and this needs further attention.

5. CONCLUSIONS

Comprehensive analysis and measurements were performed for hover and wind tunnel operation of a counter-rotating coaxial rotor system up to advance ratios of $\mu = 0.5$ and for varying lift offsets. The experimental data was obtained in the Glenn L. Martin Wind Tunnel at the University of Maryland. This paper focused on the development and validation of a CAMRAD II model of the test article using the experimental hover and forward flight wind tunnel test data, to further the understanding of the dynamics and aerodynamics of lift-offset rotors and coaxial rotorcraft operating at high advance ratios.

The following specific conclusions have been drawn:

- The rotor blade structural dynamics of the numerical model were validated by the first three flap and the first lag and torsion non-rotating natural frequencies.
- Hover performance validation was successfully performed for the isolated rotor and for the coaxial rotor system, including individual upper and lower coaxial rotor validation.
- Cyclic pitch control characteristics correctly predicted the trends of the test data, but their magnitudes were mostly underpredicted by a constant offset for the isolated rotor. The free play of the pitch control system

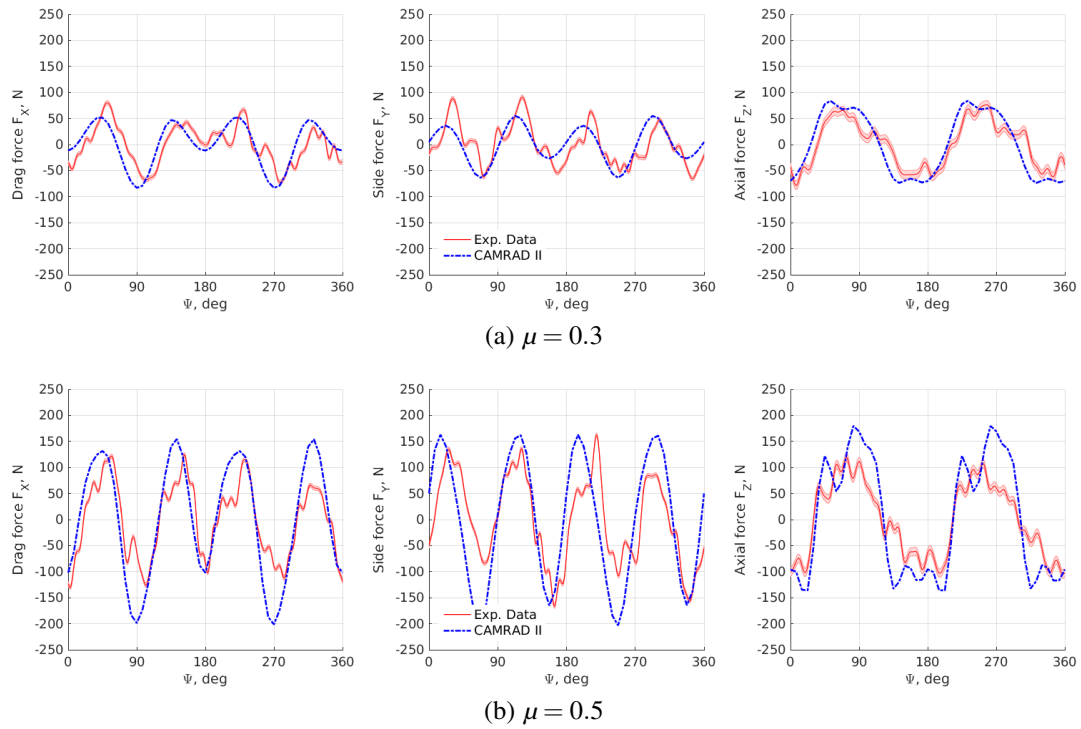


Fig. 23: Vibratory hub loads (mean removed) for the lower isolated rotor at $\Theta_0 = 8^\circ$ and zero lift offset.

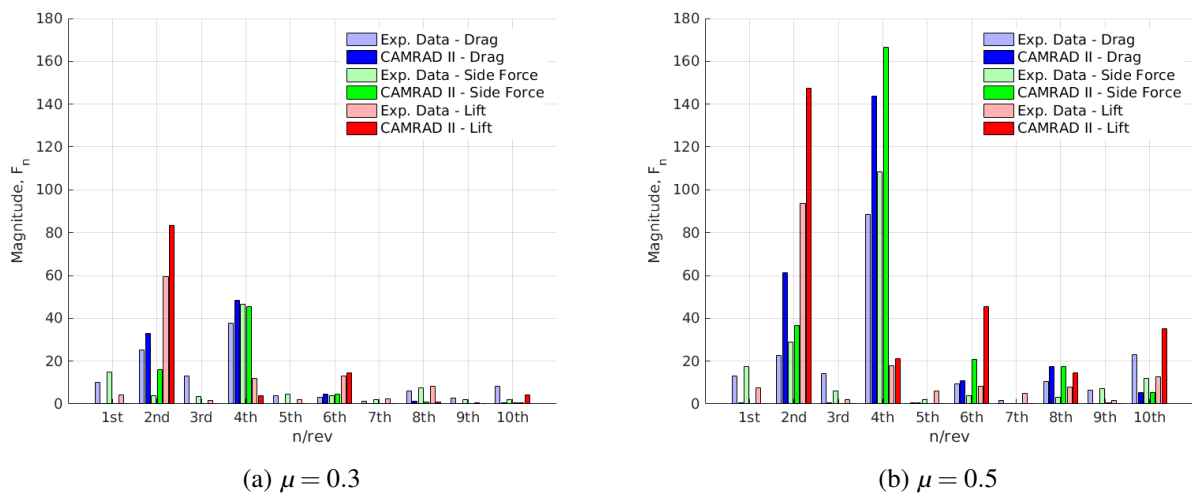


Fig. 24: Harmonic hub loads for the lower isolated rotor at $\Theta_0 = 8^\circ$ and zero lift offset.

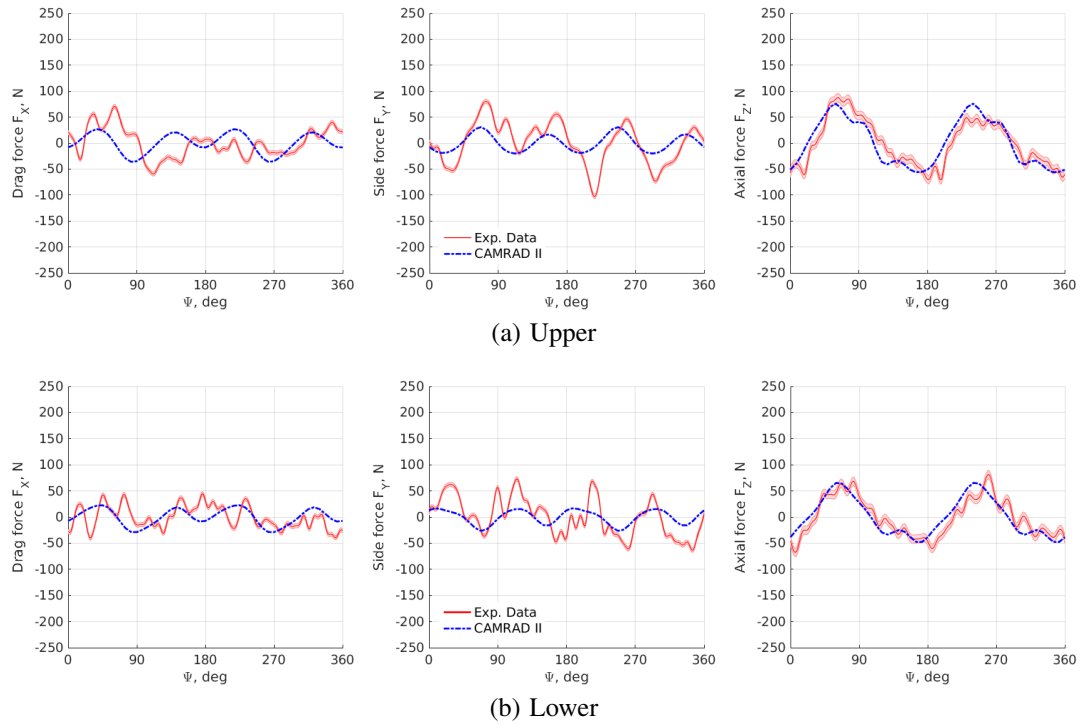


Fig. 25: Vibratory hub loads (mean removed) for the coaxial rotors at $\Theta_0 = 8^\circ$, $\mu = 0.3$ and zero lift offset.

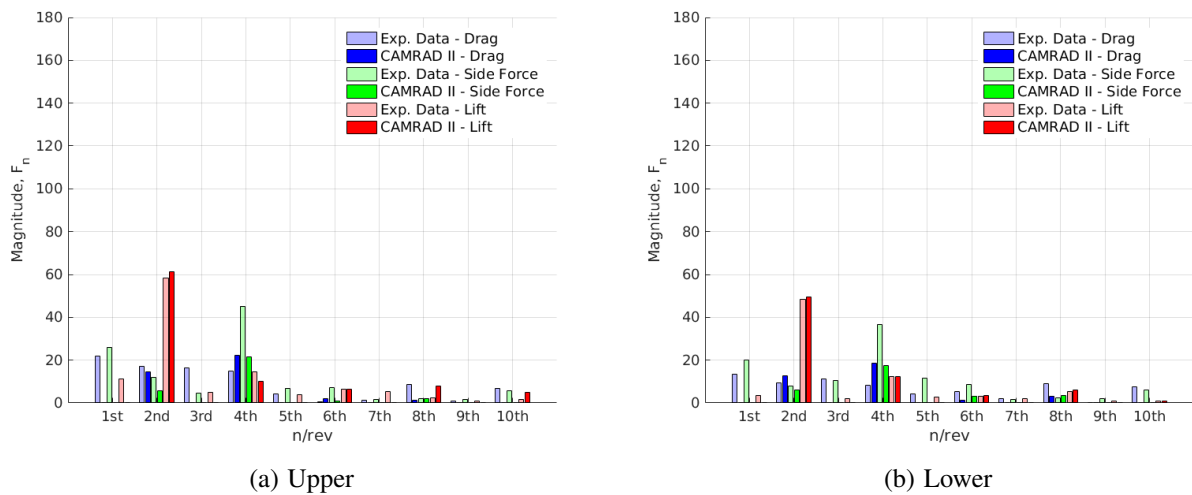


Fig. 26: Harmonic hub loads for the coaxial rotors at $\Theta_0 = 8^\circ$, $\mu = 0.3$ and zero lift offset.

and uncertainties in the pitch control calibration during the measurements may have contributed to the offset, and this will be investigated further.

- Predicted blade loading characteristics for varying lift offset and advance ratios matched the wind tunnel results well, particularly for the coaxial rotor configuration and for medium to high advance ratios ($\mu = 0.3 - 0.5$). The blade loading decreased with increasing advance ratio and it increased with lift offset.
- Rotor side force versus lift offset showed similar trends but the side force was generally underpredicted, particularly for greater lift offsets. It is unclear if the experimental data or the numerical results must be accounted for that, and this is an area of further research.
- Numerical predictions for the coaxial rotors correlated well with the measurements for blade loadings, cyclic controls and blade clearance for multiple advance ratios and varying lift-offset conditions. Differences at high lift-offset conditions may be related to the underprediction in the lateral cyclic controls.
- Isolated rotor vibratory hub loads correlated well with the wind tunnel data for multiple advance ratios. For the coaxial configuration, the axial vibratory forces correlated well, but significant higher-frequency fluctuations in the measurements made it challenging to properly validate the rotor vibratory drag (longitudinal) and side (lateral) forces.

Besides further improvement of the numerical aero-mechanics model, future work includes the evaluation of pitch link loads and also focuses on enhancing the vibratory load prediction capability for the coaxial rotor system. Experiments and analysis will be extended to advance ratios of up to $\mu = 1$. For the closely spaced rotors, aerodynamic interference is strong, which has a major impact on the vibratory loads, particularly on the lower rotor. Therefore, further analysis will also examine the effects of blade vortex interactions on the rotors' vibratory loads, including investigations of the frequency content of the loads and aerodynamic interactions. Furthermore, offloading the (coaxial) main rotor by, e.g., using additional pusher propellers for thrust compounding will be investigated. These studies of the interactional aerodynamics and dynamics of a model rotorcraft will further the understanding of such configurations, and thus, will be of interest for current and future configurations using thrust compounding.

ACKNOWLEDGEMENTS

The authors would like to thank Mr. Joseph Schmaus at the University of Maryland for providing the VR-12 airfoil tables. The experimental part of this work was supported by the U.S. Army, Navy, and NASA Vertical Lift Research Center of Excellence (VLRCOE) program with Dr. Mahendra Bhagwat serving as the technical monitor.

REFERENCES

- [1] Leishman, J. G., *Principles of Helicopter Aerodynamics*, Cambridge University Press, 2006, Chap. 10.
- [2] Bagai, A., "Aerodynamic Design of the X2 Technology Demonstrator (TM) Main Rotor Blade," American Helicopter Society 68th Annual Forum, Montreal, Canada, April 29–May 1, 2008.
- [3] Coleman, C. P., "A Survey of Theoretical and Experimental Coaxial Rotor Aerodynamic Research," NASA Technical Paper TP-3675, 1997.
- [4] Ramasamy, M., "Hover Performance Measurements Toward Understanding Aerodynamic Interference in Coaxial, Tandem, and Tilt Rotors," *Journal of the American Helicopter Society*, Vol. 60, July 2015, doi: 10.4050/JAHS.60.032005.
- [5] Juhasz, O., Syal, M., and Celi, R., "Comparison of Three Coaxial Aerodynamic Prediction Methods Including Validation with Model Test Data," AHS Aeromechanics Specialists' Conference, San Francisco, CA, January 20–22, 2010.
- [6] Leishman, J. G., and Syal, M., "Figure of Merit Definition for Coaxial Rotors," *Journal of the American Helicopter Society*, Vol. 53, July 2008, doi: 10.4050/JAHS.53.290.
- [7] Johnson, W., "Influence of Lift Offset on Rotorcraft Performance," NASA Technical Report TP-2009-215404, November 2009.
- [8] Yeo, H., and Johnson, W., "Investigations of Maximum Blade Loading Capability of Lift-Offset Rotors," American Helicopter Society 69th Annual Forum, Phoenix, AZ, May 21–23, 2013.
- [9] Passe, B., Sridharan, A., and Baeder, J., "Computational Investigations of Coaxial Rotor Interactional Aerodynamics in Steady Forward Flight," 33rd AIAA Applied Aerodynamics Conference, Dallas, TX, June 22–26, 2015.
- [10] Singh, R., Kang, H., Bhagwat, M. J., Cameron C., and Sirohi J., "Computational and Experimental Study of Coaxial Rotor Steady and Vibratory Loads," AIAA SciTech, San Diego, CA, January 4–8, 2016.
- [11] Cameron, C., Karpatne, A., and Sirohi, J., "Performance and Vibratory Hub Loads of a Mach-Scale Coaxial Rotor in Hover," American Helicopter Society 70th Annual Forum, Montreal, Canada, May 20–22, 2014.
- [12] Cameron, C., Uehara, D., and Sirohi, J., "Transient Hub Loads and Blade Deformation of a Mach-Scale Coaxial Rotor in Hover," AIAA SciTech, Kissimmee, FL, January 5–9, 2015.

- [13] Cameron, C., and Sirohi, J., “Performance and Loads of a Model Coaxial Rotor Part I: Wind Tunnel Testing,” American Helicopter Society 72nd Annual Forum, West Palm Beach, FL, May 17–19, 2016.
- [14] Schmaus, J., and Chopra, I., “Aeromechanics for a High Advance Ratio Coaxial Helicopter,” American Helicopter Society 71th Annual Forum, Virginia Beach, VA, May 5–7, 2015.
- [15] Schmaus J., and Chopra I., “Performance and Loads of a Model Coaxial Rotor Part II: Prediction Validations with measurements,” American Helicopter Society 72nd Annual Forum, West Palm Beach, FL, USA, May 17–19, 2016.
- [16] Blackwell, R., and Millott, T., “Dynamic Design Characteristics of the Sikorsky X2 TD Aircraft,” American Helicopter Society 65th Annual Forum, Montreal, Canada, April 29–May 1, 2008.
- [17] Walsh, D., Weiner, S., Arifian, K., Bagai, A., Lawrence, T., and Blackwell, R., “Development Testing of the Sikorsky X2 Technology™ Demonstrator,” American Helicopter Society 65th Annual Forum, Fort Worth, TX, May 27–29, 2009.
- [18] Johnson, W., “Technology Drivers in the Development of CAMRAD II,” American Helicopter Society Aeromechanics Specialists’ Conference, San Francisco, CA, January 19–21, 1994.
- [19] Bagai, A., and Leishman, J. G., “Rotor Free-Wake Modeling Using a Pseudo-Implicit Technique – Including Comparisons With Experimental Data,” *Journal of the American Helicopter Society*, Vol. 40, July 1995, doi: 10.4050/JAHS.40.29.
- [20] Leishman, J. G., Bhagwat, M. J., and Bagai, A., “Free-Vortex Filament Methods for the Analysis of Helicopter Rotor Wakes,” *Journal of Aircraft*, Vol. 39 (5), May 2002, doi: 10.2514/2.3022.
- [21] Lim, J. W., McAlister, K. W., and Johnson, W., “Hover Performance Correlation for Full-Scale and Model-Scale Coaxial Rotors,” *Journal of the American Helicopter Society*, Vol. 54, July 2009, doi: 10.4050/JAHS.54.032005.
- [22] Lim, J. W., Yu, Y. H., and Johnson, W., “Calculation of Rotor Blade–Vortex Interaction Airloads Using a Multiple-Trailer Free-Wake Model,” *Journal of Aircraft*, Vol. 40 (6), Nov-Dec 2003.
- [23] Johnson, W., *Rotorcraft Aeromechanics*, Cambridge University Press, 2013.
- [24] Feil, R., Rauleder, J., and Hajek, M., “Aeromechanics Analysis of a Coaxial Rotor System in Hover and High-Advance-Ratio Forward Flight,” 34th Applied Aerodynamics Conference, AIAA Aviation, Washington, DC, June 13–17, 2016.
- [25] Hoad, D. R., “Helicopter Blade-Vortex Interaction Locations – Scale-Model Acoustics and Free-Wake Analysis Results,” NASA Technical Paper 2658, Dallas, AVS-COM Technical Memorandum 87-B-1, 1987.